JOURNAL OF PROPULSION AND POWER
Vol. 23, No. 1, January–February 2007

Development of a Dynamometer for Measuring Small Internal-Combustion Engine Performance

Shyam Menon,* Nathan Moulton,* and Christopher Cadou†
University of Maryland at College Park, College Park, Maryland 20742

DOI: 10.2514/1.19825

Small hobby engines with masses less than 1 kg are attractive for use in low-cost unmanned air vehicles, because they are mass-produced and inexpensive. However, very little information about their performance is available in the scientific literature. This paper describes the development of a dynamometer system suitable for measuring the power output and efficiency of these small engines and presents detailed performance measurements for a particular engine with a mass of 150 gm that could be suitable for powering a low-cost unmanned air vehicle. When the mixture setting is adjusted according to the manufacturer's instructions, the peak power of this engine is 112 W at 9450 rpm with a brake specific fuel consumption of 3.0 kg/kWh. The performance can be improved to 159 W at 12,000 rpm and brake specific fuel consumption of approximately 2.1 kg/kWh by controlling the mixture.

Nomenclature

$\boldsymbol{F}$	=	force
f_a, f_m	=	atmospheric factor and engine factor
I	=	moment of inertia
k_{lc}	=	stiffness of the load cell
L/D	=	lift/drag ratio of the vehicle
m	=	mass of the additional weight added to the engine cradle
$\dot{m}$	=	mass flow rate
N_{nat}	=	engine speed associated with the natural frequency of the cradle-load cell system
P	=	measured output power
P_r	=	corrected power under standard reference conditions
p, p_r	=	test pressure and standard reference pressure
p_{sr}, p_s	=	test saturated water vapor pressure and standard reference saturated water vapor pressure
Q_r	=	heating value
q	=	fuel mass per cycle per liter of air
q_c	=	corrected specific fuel delivery
R	=	length of the moment arm
r	=	distance between added mass and cradle axis of rotation
r_r	=	boost pressure ratio
T_r, T	=	test ambient air temperature and standard reference ambient air temperature
α_c	=	atmospheric correction factor
β	=	overall damping coefficient for cradle bearings
Γ	=	measured engine torque
δ_{max}	=	maximum deflection of the load cell
η	=	efficiency
θ_e	=	angle of cradle associated with steady state operation
ρ	=	density of air, mixture, methanol, nitromethane, and castor oil
ϕ_r, ϕ	=	test relative humidity and standard reference relative humidity
χ	=	volume fraction of methanol, nitromethane, and castor oil in the fuel
χ_f	=	fuel mass fraction at takeoff
ω	=	engine speed
ω_n	=	natural frequency of the system

Subscripts

a	=	air
CH_3OH	=	methanol
CH_3NO_2	=	nitromethane
c	=	cradle
e	=	engine
f	=	fuel
lc	=	load cell
o	=	overall
oil	=	castor oil
p	=	propulsive
th	=	thermal

I. Introduction

THE drive to build small, inexpensive unmanned air vehicles (UAVs) is creating a demand for compact, inexpensive powerplants that are thermodynamically efficient and consume high energy-density liquid hydrocarbon fuels. An example of such a vehicle is the low-cost UAV called the Silver Fox[‡] that is being manufactured for the U.S. Navy by Advanced Ceramics Research, Inc. Maximizing the range and/or endurance of these vehicles requires knowledge of the propulsive efficiency of the propeller and the thermal efficiency [or brake specific fuel consumption (BSFC)] of the engine [1]. If the vehicle is equipped with a fixed-pitch propeller (as are most small UAVs), knowledge of the entire operating map of the engine is required to optimize the efficiency of the engine-propeller combination [2]. Although small internal-combustion engines developed to power model aircraft could be well suited for powering small UAVs because they are mass-produced and relatively inexpensive, their present utility is limited by a lack of reliable performance information and the fact that most of these engines do not operate on practical fuels like JP-8.

An additional motivation for acquiring reliable performance data for a range of differently sized small engines is to develop improved understanding of how engine performance scales with size. Theoretical analyses based on system-level thermodynamic considerations [3,4] and combustion quenching [5] indicate that the minimum size of a heat engine is on the order of 1 mm^3. Other studies that include the effects of friction and leakage in reciprocating

Received 1 September 2005; accepted for publication 6 May 2006.

*Graduate Student, Department of Aerospace Engineering.
†Assistant Professor, Department of Aerospace Engineering. Senior Member AIAA

‡Data available online at http://www.acrtucson.com/UAV/silverfox/index.htm [cited 2 June 2005].

engines arrive at similar conclusions [6]. Because 1 mm [3] is not much smaller than the devices that some microengine programs [7,8] are attempting to construct and is only about a factor of 10 smaller than the smallest hobby engines available today, an investigation of how the performance of small engines changes as one approaches this theoretical limit would be useful. Studies of complete engines also have the advantage of being able to capture the integrated effects of technological factors like engine configuration, timing, machining process, surface friction, heat loss, etc., that are hard to treat collectively through modeling. Thus, investigations of small engine performance may also make it possible to determine the relative importance of thermodynamic vs technological factors on the minimum size of a practical power system.

Aside from the efforts of one research group [9,10] and some simple measurements reported by designers of small UAVs [11], there appears to be very little detailed information on the performance of small hobby engines in the scientific literature. In contrast, hobby magazines have published many reviews of small engine performance over the years [12–17], but the data they provide are incomplete. At most, power output and torque as a function of engine rpm at wide open throttle is reported. Fuel consumption is seldom reported (we were able to find one example [18]), and other parameters like air flow rates, cylinder head temperatures, and fuel/air ratios seem not to be reported at all.

Performance data reported by the engine manufacturers are less complete than that reported by the hobby magazines and are usually limited to peak power at a particular engine speed. Specific fuel consumption or efficiency is not reported at all, because it is usually of no concern to hobbyists. Furthermore, the quality of this information is difficult to evaluate given that quoted power outputs for engines with the same displacement vary widely from manufacturer to manufacturer.

The work presented here describes the development of a small dynamometer system suitable for acquiring the detailed and reliable engine performance data that are necessary to develop optimized small UAVs and to develop an understanding of how engine performance scales with size. The principal measurements provided by the system are engine torque, engine speed, fuel mass flow rate, and air mass flow rate. The power output of the engine is given by

$$P = \Gamma\omega \tag{1}$$

and the overall efficiency (or fuel conversion efficiency [19]) of the engine is given by

$$\eta_o = P/\dot{m}_f Q_r \tag{2}$$

The efficiency of the engine is also reported in terms of the brake specific fuel consumption, which is given by [20]

$$\text{BSFC} = \dot{m}_f/P \tag{3}$$

BSFC is usually reported in g/kWh (or lb/hp · h).

II. Challenges

Table 1 presents estimates for the power, speed, and fuel flow rate that are expected for several small engines that could be used to power small UAVs. Most of these estimates come from engine manufacturers' information, but torque and fuel consumption are estimated using methods reported elsewhere [21]. The entries in the table show that several factors complicate performance measurements in these small engines. First, operating speeds are relatively high, which means that high-speed transmissions are required if propellers are not used to apply loads to the engine. Second, fuel flow rates are small and not in a range that is accessible by most off-the-shelf liquid flow meters. The fuel flow measurement is complicated further by the fact that the pressure losses through the flow meter must be very small so as not to starve the engine of fuel. The pressure driving the fuel flow in the engine being considered here ranges from 3 to 7 KPa and so losses through the flow meter should be <0.03 KPa. Third, engine torque levels are low, but ambient noise (vibration) levels are high, because all of these small engines are single-cylinder designs. As a result, care must be taken to damp strong 1/rev (for two-cycle engines) and 1/2rev (for four-cycle engines) disturbances and to avoid exciting resonant modes of the measurement system. At best, failure to control vibration degrades the accuracy of the torque measurement by raising background noise around a small torque signal. At worst, it can destroy the torque/force sensor. Finally, the dynamometer system must be mechanically flexible so as to accommodate a wide range of engines with minimal mechanical modifications.

Given these challenges, our objective is to determine power output and efficiency to within 10% of their nominal values. This level of accuracy should be adequate for guiding engine selection for low-cost UAVs and should provide adequate discrimination between engines of different sizes, so that scaling laws can be identified.

III. Dynamometer System

There have been a number of articles in the hobby literature describing various dynamometer systems [22–24][§],[¶],[**] for measuring engine performance. All measure engine torque by measuring the torque reaction at the engine mounts. In most of these, the load is generated by a propeller attached to the engine, although one specifically designed to measure transient performance uses a set of flywheels.[††] The approach taken here is to measure torque at the engine supports, but to use a hysteresis brake to apply the load. The advantages of the hysteresis brake are that it is continuously adjustable (so that complete power curves can be acquired without the need to shut the engine down), the applied torque is independent of the operating speed of the engine, and the brake is electrically controlled (so that it may easily be incorporated into control systems like those found in conventional dynamometers).

Figure 1 is a photograph of the dynamometer illustrating the major components. The engine to be tested is mounted in a cradle that is supported on precision low-breakaway torque bearings ($<1.41 \times 10^{-4}$ N · m or 0.02 oz · in.) about an axis coincident with the engine's axis of rotation. The cradle is prevented from rotating by a Sensotek model 31 load cell that anchors it to the cradle support. The full-scale capacity of the load cell is 22.2 N (5 lb). The absorber is a Magtrol model HB-880 double hysteresis brake. It is connected to the engine through a gear system and provides a continuously variable load to the engine. As the load is applied, the engine reacts against the cradle, causing a load to be exerted on the load cell. The product of the load cell force and the moment arm length gives the engine torque.

This torque measurement scheme has several advantages. First, by measuring the reaction of the engine at its supports, and not downstream at the absorber as is done on larger dynamometers, no accounting needs to be made for losses in the power train. Second, using a load cell and adjustable moment arm as opposed to a dedicated torque sensor means that the sensitivity of the instrument may be adjusted for different engines simply by attaching the load cell to the moment arm at different radial locations. This also means that a single load cell can be used to test a relatively wide range of engines.

A small model aircraft engine made by AP Engines (Yellowjacket, 2.45 cm^3, 150 g) is used in this work to evaluate the performance of the dynamometer system. It corresponds to entry number 1 in Table 1. The throttle is controlled remotely using a Futaba servo, FM receiver, and battery, all of which are attached to the cradle. This enables throttle adjustments to be made without affecting the torque measurements. Cylinder head temperature is measured using a stainless-steel-sheathed K-type thermocouple held in contact with one of the cylinder head bolts. A similar thermocouple inserted into

[§]Data available online at http://www.clcombat.info/dyno.html [cited 8 July 2005].

[¶]Data available online at http://www.control-line-team.de/motorenpruefstand/motorenpruefstand_en.html [cited 8 July 2005].

[**]Data available online at http://rcboat.com/dyno.htm [cited 8 July 2005].

[††]Data available online at http://rcboat.com/dyno.htm [cited 8 July 2005].

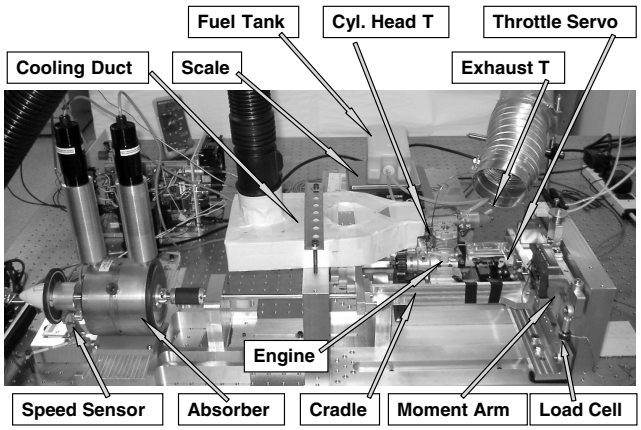

Fig. 1 Photograph of dynamometer system showing the important components.

the muffler exit measures exhaust gas temperature. Although both thermocouples are terminated on the cradle support, the forces exerted by their tips have negligible impacts on the torque measurement.

The engine is operated on glow fuel that is a mixture of 10% nitromethane, 20% castor oil, and 70% methanol. The heating value of the mixture was measured by a commercial fuel testing laboratory using standard procedures [25] and found to be 21.82 MJ/kg. Table 2 gives the composition and density of the fuel mixture as well as an estimate of the mixture's overall heating value based on the heating values of the individual constituents. Note that we were unable to find a reference for the heating value of castor oil, and so the value of 29.9 MJ/kg was chosen to match the measured heating value of the mixture.

The balanced chemical reaction for the complete combustion of the fuel with air (assuming that the castor oil acts only as a lubricant and is therefore inert) is given by

$$A\,\mathrm{CH_3OH} + B\,\mathrm{CH_3NO_2} + \mathrm{C\,Oil} + f(0.21\mathrm{O_2} + 0.79\mathrm{N_2}) \rightarrow (A+B)\mathrm{CO_2} + [(4A+3B)/2]\mathrm{H_2O} + 0.79x\,\mathrm{N_2} + \mathrm{C\,Oil} \quad (4)$$

where $A = \chi_{\mathrm{CH_3OH}}\rho_{\mathrm{CH_3OH}}/MW_{\mathrm{CH_3OH}}$, $B = \chi_{\mathrm{CH_3NO_2}}\rho_{\mathrm{CH_3NO_2}}/MW_{\mathrm{CH_3NO_2}}$, and $C = \chi_{\mathrm{oil}}\rho_{\mathrm{oil}}/MW_{\mathrm{oil}}$. The first set of constituents in parentheses in Eq. (4) is the fuel mixture and the second set in parentheses is the air. Equation (4) gives a stoichiometric fuel/air ratio of 0.152 (or 0.227 on a mass basis). Assuming that the castor oil is inert lowers the effective heating value of the fuel mixture to 15.2 MJ/kg. However, we use the measured heating value of 21.82 MJ/kg to compute the overall efficiency, because the unburned lubricant represents energy that is wasted and we have no means to determine how much of the lubricant may have reacted. The degree to which the castor oil reacts also has a strong impact on the operating equivalence ratio. For example, if 100% reacts, the stoichiometric fuel/air ratio becomes 0.096 (or 0.144 on a mass basis).

The fuel flow rate is measured using an FMTD4 nutating microflowmeter manufactured by DEA Engineering. The meter is a positive displacement type that produces a series of 5-V pulses, each of which corresponds to the passage 0.02 cm^3 of fluid. Two flexible hoses connect the tank to the engine on the cradle. One carries the fuel to the needle-valve inlet. The other extends from a fitting on the muffler back to the fuel tank, so that pressure in the exhaust manifold drives fuel from the tank into the engine. The forces exerted by the hoses on the cradle do impact the torque measurement, but this is accounted for by calibrations performed before and after every run. The fuel pressure in the tank is monitored using an Omega PX139 series differential pressure transducer with a range of ± 103.4 kPa (15 psi).

Table 2 Properties of glow fuel constituents and mixture

Component	χ	ρ, g/cm^3	Q_r, MJ/kg
CH_3COH	0.7	0.81	21.12
CH_3NO_2	0.1	1.13	11.6
Castor oil ($C_{18}H_{34}O_3$) [26]	0.2	0.96	44
Mixture	1.0	0.875	21.8
Mixture (oil inert)	1.0	0.875	15.2

Air flow rate is measured using a TSI model 4021 mass flowmeter that has an operating range of 0–300 standard l/min and a linear 0–4 V dc output signal. Because the flow sensor only works properly under steady flow conditions, a plenum is placed between the flowmeter and the engine to damp out fluctuations. These fluctuations are a strong and inherent feature of many scavenged two-stroke engines, which is caused by the opening and closing of valves in the engine. A flexible tube connects the plenum to the carburetor to minimize the impact on the torque measurements. Parasitic torque associated with the tube is accounted for during the calibration of the cradle. The volume of the plenum is considerably larger than (3000 times) the displacement of the engine being tested to provide maximum damping of flow oscillations and minimum pressure loss. The length of the tube is also kept as short as possible to minimize pressure loss. The total pressure loss through the plenum and tube is less than 0.01% at the maximum flow rate.

The maximum operating speed of the absorber is 8000 rpm. Because the maximum operating speed of the engine is 16,000 rpm, a 2.5:1 transmission is used to connect the brake to the engine. The torque applied by the brake is continuously adjustable from zero to its maximum rating by changing the current supplied to the brake's magnetic coils. A dc source supplies the current and can be controlled from a panel-mounted potentiometer or a 0–5 V analog signal. The brake is rated to dissipate up to 800 W of power without forced air cooling. More power can be dissipated on an intermittent basis or if cooling air is provided. Two infrared thermocouples monitor the temperatures of the brake drums. So far, it has not been necessary to actively cool the brakes.

Engine speed is measured using an off-the-shelf system manufactured by ElectroSensors. It consists of a magnetic pulser disc (containing 16 alternating poles) that is attached to the absorber shaft, a proximity sensor that detects the passage of these poles, and a model SA420 signal conditioner that outputs an analog voltage proportional to frequency. The engine speed is that reported by the speed sensor multiplied by the gear ratio of the transmission (which, in this case, is 2.5). The accuracy of the speed measurement system is $\pm 0.1\%$ of the speed value.

A model aircraft propeller nose cone attached to the end of the absorber shaft permits the engine to be started using a conventional model aircraft starter. Cooling air for the engine is provided by a specially constructed duct that directs air from a blower around the

Table 1 Data and performance estimates for several single-cylinder model aircraft engines that could be appropriate for powering a low-cost UAV

	Weight, g	Cycle	Rated power, W	Rated speed, krpm	Displacement, cm^3	Fuel flow, g/s
1	150.2	2	186.43	15	1.47	0.65
2	269.3	2	745.7	15	6.55	2.87
3	374.2	2	1208	16	7.54	3.53
4	402.56	4	671.1	12	8.52	1.5
5	629.3	4	1193.1	12	14.91	2.62

moving parts of the cradle and directly across the cylinder head. The engine will overheat rapidly without the cooling air.

IV. Data Acquisition

A LabVIEW data acquisition system is used to condition and log signals from all of the sensors. Analog signals are amplified and low-pass filtered using a National Instruments SCXI 1327 instrumentation amplifier. Thermocouple signals are amplified by a National Instruments SCXI 1112 thermocouple amplifier. Analog-to-digital conversions are performed using an 8-channel, 16-bit A/D card resident in a PC. Pulses from the flow meter are counted using a TDS 3034B digital oscilloscope and converted into flow rate using the sensor's calibration factor. Data are acquired in a 1-Hz strip-chart mode that provides a record of everything that happened during the course of the experiment and in a burst mode at specific operating points for which each channel is sampled 1000 times at 1 kHz, so that random fluctuations may be averaged out.

V. Vibration Control

The intermittent pressure in the combustion chamber leads to strong 1/rev and 1/2rev disturbances that can excite resonances in the cradle-load cell system. These disturbances decrease the signal-to-noise ratio of the measurement and, if left unchecked, can damage or destroy the load cell. The engine speed associated with the natural frequency of the cradle-load cell system is given by

$$N_{\text{nat}} = \frac{60}{2\pi}\omega_n \tag{5}$$

where $\omega_n = \sqrt{k_{\text{lc}}R^2/I}$. Ideally, the engine-cradle system would be designed so that N_{nat} is significantly greater than $N_{\max}$, the engine's maximum operating speed, so that resonances of the cradle/load cell system could not be excited. In practice, however, keeping ω_n high is difficult. The physical size of the engine places a lower bound on the total moment of inertia while the load cell is relatively compliant. Any structure associated with the cradle increases I and lowers ω_n further.

The approach taken here is to increase the I of the system and decrease the R, so that the operating speed of the engine corresponds to a high-order mode of the cradle-load cell system that will be more highly damped. Accordingly, 5.4 kg has been added to the cradle at 15.88 cm (6.25 in.) from the cradle's axis of rotation, and a moment arm of 3.81 cm (1.5 in.) is used. Although this strategy is not ideal, because the engine must traverse the fundamental frequency as it accelerates to operating speed, locking the cradle down and releasing it after the engine has traversed the fundamental has prevented resonance-induced damage to the sensor.

VI. Measurements

A. Torque Measurement

Figure 2 is a free-body diagram showing the relationship between the torques and forces acting on the cradle. The x and y axes are located at the center of rotation of the cradle and the z axis extends along the cradle's axis of rotation. A force balance on the cradle leads to the following expression for the torque Γ_e exerted by the engine on the cradle:

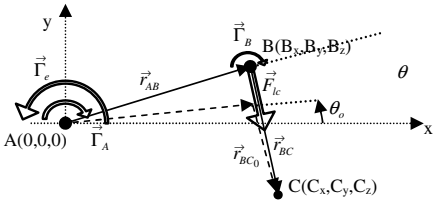

Fig. 2 Vector diagram showing the forces acting on the torque-measuring cradle and the mechanical constraints imposed on the cradle/load cell system.

$$\Gamma_e = \Gamma_A + \Gamma_B - \boldsymbol{r}_{AB} \times \boldsymbol{F}_{\text{lc}} \tag{6}$$

Γ_A and Γ_B are, respectively, the parasitic torques associated with the cradle bearing and the load cell attachment points. The moment arm is represented by $\boldsymbol{r}_{AB}$, which extends from the cradle's center of rotation A to the load cell attachment point B. The cradle is constrained by $\boldsymbol{F}_{\text{lc}}$, which acts along the load cell axis $\boldsymbol{r}_{BC}$. The objective is to use the measurements of $|\boldsymbol{F}_{\text{lc}}|$ made by the load cell to determine the torque produced by the engine. The complete solution to Eq. (6) accounts for the fact that the load cell is not infinitely stiff and deflects in response to the applied load. Although this can be important in situations in which the load cell is attached to the cradle via an elastomeric element (some dynamometer designs use these to dampen vibrations), the load cell used here only deflects a few thousandths of an inch. As a result, treating $\boldsymbol{r}_{AB}$ as a constant does not have a significant impact on the measured torque. The complete solution to Eq. (8) when deflection of the load cell is important is presented elsewhere [21]. Because $\boldsymbol{r}_{AB}$ is constrained to the x–y plane, it can be written in terms of a single independent variable θ_e, the angle of the cradle,

$$\boldsymbol{r}_{AB} = R\cos\theta_e\hat{\boldsymbol{i}} + R\sin\theta_e\hat{\boldsymbol{j}} + \hat{\boldsymbol{k}} \tag{7}$$

where $\hat{\boldsymbol{i}}$, $\hat{\boldsymbol{j}}$, and $\hat{\boldsymbol{k}}$ are unit vectors associated with the x, y, and z directions, respectively. The parasitic torques exerted at the cradle bearings A and the load cell attachment B are estimated using the measured breakaway torque. Note that only components of torque that act along the cradle axis are considered. All other components are assumed to be negligible. Table 3 shows parameter values for the torque measurement system.

The primary source of uncertainty in the torque measurement arises from the 0.21% of full-scale (FS) uncertainty in the load cell reading. Accordingly, the best accuracy is obtained by choosing a moment arm length that maximizes the force exerted on the load cell. The difficulty, of course, is that often the torque is not known until after the experiment is performed. Replacing the 22.2 N cell with a more sensitive unit would permit the measurement of smaller torques to better than 0.5%.

B. Corrected Performance

Because engine performance varies with the condition of the atmosphere (pressure, temperature, and humidity), it is corrected to standard atmospheric conditions, so that measurements made on different days may be compared. The methods for accomplishing this are well known [27], and are summarized in the following discussion, in which the subscripted terms correspond to the reference conditions and the nonsubscripted terms correspond to test conditions.

A correction factor α_c times the measured power gives the power P_r:

$$P_r = \alpha_c P \tag{8}$$

The correction factor for a naturally aspirated compression ignition engine depends on the atmospheric factor and the engine factor:

$$\alpha_c = (f_a)^{f_m} \tag{9}$$

The atmospheric factor accounts for the effects of atmospheric pressure, temperature, and the relative humidity. It is computed as follows:

$$f_a = \left(\frac{p_r - \phi_r p_{\text{sr}}}{p - \phi p_s}\right)\left(\frac{T}{T_r}\right)^{0.7} \tag{10}$$

The engine factor for a two-stroke engine is [27]

$$f_m = 0.036q_c - 1.14 \tag{11}$$

$$q_c = q/r_r \tag{12}$$

Table 3 Parameter values for torque measurement system

Parameter	Value	Uncertainty	Unit
R	0.635–13.3	±0.005	cm
$\|\boldsymbol{F}_{\text{lc}}\|$	0–22.25	±0.21%FS	N
$\delta_{\max}$	0.012–0.05	±0.025	mm
k_{lc}	174,880–437,200	±218, 600	N/m
θ_0	0	±5	deg
C_x	0.6–13.3	±0.005	cm
C_y	−10.16	±0.005	cm
C_z	0	±0.0012	m
$\Gamma_A \circ \hat{\boldsymbol{k}}$	1.4e − 3	±1.4e − 3	N · m
$\Gamma_B \circ \hat{\boldsymbol{k}}$	<1.4e − 3	±1.4e − 3	N · m
I_e	>0.0142	±0.0142	N · m^2
I_c	>0.0854	±0.0142	N · m^2
m	11.93	±0.1133	N
r	0.1	±0.0002	m

Table 4 Results of uncertainty analysis for a typical engine performance point

	Value	Uncertainty	Unit	Uncertainty (%)
F_{lc}	1.598	0.04	N	2.5
ω	10,009.12	27.86	rpm	0.278
$\dot{m}_f$	0.1269	0.00095	g/s	0.75
P	63.58	5.4	W	8.5
Γ_e	0.0609	0.005	N · m	8.46
η_o	2.29	0.204	%	8.9

where q is set by the fuel/air ratio and r_r is the ratio of the pressure of the charge entering the cylinder to atmospheric pressure. It equals one for the loop-scavenged engines considered here.

C. Uncertainty Analysis

The uncertainty analysis follows standard procedures [28] for determining the 95% confidence interval for a particular measurement. Sample results presented in Table 4 show that uncertainty in the torque measurement is the most important contributor to uncertainty in the power and efficiency measurements.

VII. Experimental Procedure

A. Calibration

The torque-measuring system is calibrated before and after each experiment by running the data acquisition program while attaching a series of known weights to the moment arm at known locations. The calibration plot of voltage vs applied load is linear, but the y intercept shifts slightly (4% on average) after the engine has been run. This shift is the largest contributor to the uncertainty in the torque measurement.

B. Operation

The cradle is clamped to the cradle support before starting the engine. This prevents damage to the load cell during engine startup as the engine accelerates through the natural frequency of the cradle-load cell system. Once the engine is started, the cradle is unlocked and the engine is leaned according to the manufacturers' instructions. This involves closing the needle valve that meters the fuel until the engine speed peaks and then reopening it by about 1/4 turn. Failing to reopen the valve (richen the mixture) can cause the engine to overheat. In one case, operating too lean actually burned a hole through a piston. The needle valve ends up being open approximately 1.5 turns after the leaning procedure is complete. Although it can be difficult to obtain repeatable mixture settings by counting needle valve turns, it is common practice in most small engines, because they are not usually equipped with fuel and air mass flow meters or oxygen sensors in the exhaust.

Data are acquired using two methods. In the first, the throttle is held at a fixed position and the mixture setting, after being adjusted per factory instructions, is held constant. The current to the hysteresis brake is then varied to apply various loads to the engine. Once the engine speed has stabilized after a change in the brake current, a burst of data from all of the sensors is acquired. Efficiency is computed using Eqs. (1) and (2) and power curves are determined by measuring torque and engine speed at different loads. In the second method, the throttle remains at a fixed position, but the load and mixture settings are varied manually to maintain a constant engine speed. These measurements are repeated for different engine speeds to obtain the operating map at fixed throttle position.

The cradle is relocked to the cradle support before the fuel is exhausted or the engine is shut down. This prevents possible damage to the load cell as the engine decelerates through the fundamental resonant frequency of the cradle-load cell system. After the engine stops, the cradle is unlocked and a second calibration of the torque-measuring system is performed.

VIII. Results And Discussion

Figures 3 and 4 show the time history of some of the various sensor readings accumulated in the strip-chart file over the course of a typical experiment. The bottom four curves in Fig. 4 show exhaust gas, cylinder head, hysteresis brake, and ambient air temperatures, and the uppermost curve shows the command voltage applied to the hysteresis brake power supply. Because increasing the command voltage increases the load on the engine, the latter curve provides a visual indication of the load cycle applied to the engine. The engine is started under no-load conditions and so the initial engine speed is high: about 11,500 rpm. Engine speed then decreases as the load is applied.

The relatively large fluctuations in the torque shown in Fig. 3 are a result of vibrations in the system and demonstrate the importance of averaging large numbers of samples to reduce the random component of the error. The flat spots on the brake command voltage trace show where the engine was allowed to come to equilibrium with the load and where bursts of data were acquired for the purpose of averaging. These averaged values are used to compute the power and efficiency curves of the engine.

The temperature of the hysteresis brake rotor rises over the course of the experiment as the power produced by the engine is converted

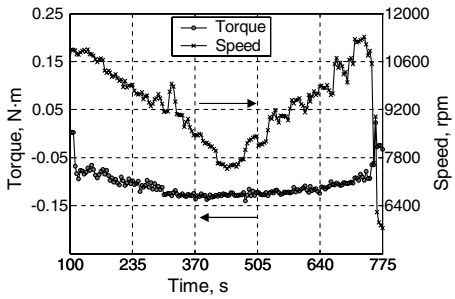

Fig. 3 Time history of engine torque and speed. The throttle is fully open and the mixture is leaned per factory instructions.

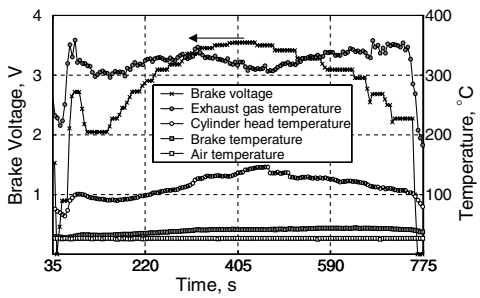

Fig. 4 Time history of brake temperature, cylinder head temperature, exhaust gas temperature, room temperature, and brake voltage from a test of the AP Yellowjacket engine.

to heat in the brake that is dissipated via transfer to the environment. As the engine speed decreases, the fuel/air ratio decreases and there is a higher heat release per power stroke. This raises the cylinder head temperature. The temperature measured by the exhaust gas thermocouple, however, is strongly influenced by heat transfer processes in the muffler. At lower speeds, the residence time in the muffler is higher and there is more time for the exhaust gases to lose heat. As a result, lower engine speeds actually result in lower temperatures of the gas exiting the muffler, even though the temperature of the gas entering the muffler (from the cylinder) is higher.

Figure 5 shows engine torque, corrected power, fuel/air ratio (mass basis), and efficiency at wide open throttle (WOT) as a function of engine speed. Data for two engines of the same model are presented. This was done to characterize the repeatability of the instrument as well as to check the variation in performance across engines due to manufacturing tolerances. Data are presented from three separate experiments on one engine in which the mixture setting was adjusted per the engine manufacturer's instructions. The same data were then obtained from another engine of the same model for two different runs. The data show that torque decreases monotonically with increasing engine speed, whereas corrected power output peaks near the middle of the operating range (around 10,000 rpm for the first engine). For the second engine, power peaks at about 12,000 rpm. The fuel flow rate increases with engine operating speed, because bleed gases from the exhaust manifold are used to pressurize the fuel tank. The increase in fuel flow rate is faster than the increase in air flow rate and the net result is the linear increase in fuel/air ratio, with engine speed shown in the figure. Although this could be advantageous (and possibly necessary) from the point of view of engine cooling, it significantly reduces the engine's overall efficiency. The overall efficiency peaks at approximately 8% at 7500 rpm and decreases linearly with engine speed. The overall efficiency at peak power is approximately 6%. These numbers are much lower than the approximately 30% overall efficiency achieved by general aviation engines when properly leaned.

The data are repeatable within their respective uncertainty intervals, with the torque measurement showing both the largest uncertainty and the largest variation between experiments. The majority of the variation between experiments is caused by the drift in torque sensor calibration occurring over the course of an experiment and small variations in needle-valve adjustment between runs. An additional contributor is variations in atmospheric conditions, which are not accounted for in the torque data presented in Fig. 5, but are accounted for in the power measurements. As a result, the variability in power is somewhat less. Finally, the data show that the largest source of variability appears to be the engines themselves, as performance varies significantly between engines of the same make and model operating on the same fuel at the same mixture setting. The reasons for this variability are not known, but they would need to be identified and corrected before these engines could be used as reliable power sources for UAVs.

Figure 6 shows engine performance as a function of engine speed at WOT for two different mixture settings. The factory mixture setting corresponds to a run in which the mixture is set per the engine manufacturer's instructions ($\sim$1.5 turns), whereas the rich setting corresponds to a run in which the mixture valve is opened more widely (2 turns), so that the fuel/air ratio is higher than normal. The exhaust gas temperature (EGT) measurements in Fig. 7 suggest that less torque and power are produced under rich conditions, because the combustion temperature is lower and, therefore, the pressure in the cylinder is lower. However, cylinder pressure measurements are required to confirm this. The data also show, as expected, that increasing the mixture setting (i.e., richening the mixture) increases the fuel/air ratio and decreases the engine efficiency.

Finally, it should be pointed out that the measurements presented in Fig. 5 are significantly different from those associated with the factory setting in Fig. 6, in spite of the fact that, in both cases, the

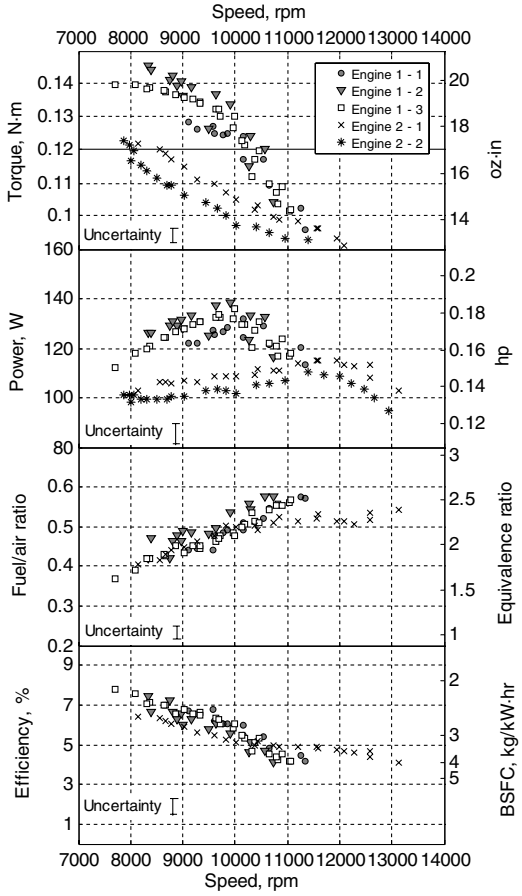

Fig. 5 Engine performance at constant mixture setting and WOT; two different engines and five different tests.

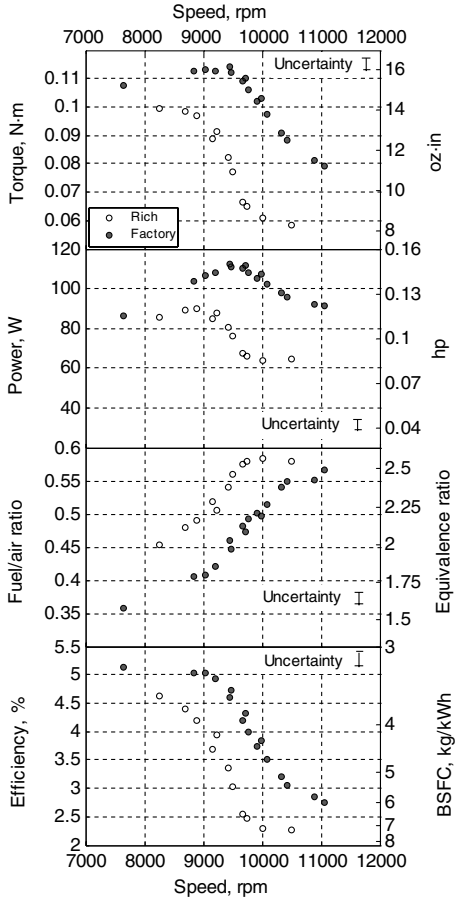

Fig. 6 Engine performance for two mixture settings at WOT.

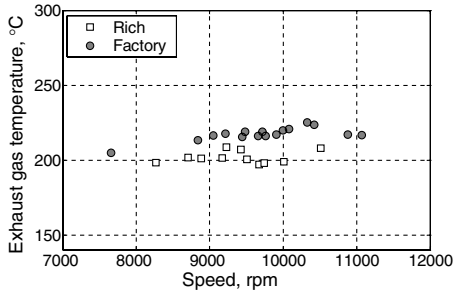

Fig. 7 Exhaust gas temperatures for two different mixture settings.

mixture was adjusted according to factory instructions. The reason is that following the factory instructions [which tell the operator to adjust the mixture for maximum rpm (as determined by the engine sound) and then open the mixture valve a specified amount (in this case, 1/4 turn)] does not lead to very repeatable needle-valve settings. The results presented in Fig. 5 were obtained by taking great care to ensure that the mixture valve opening was the same in all experiments.

Figures 5 and 6 show that power and torque decrease with increasing speed over most of the engine's operating range. This trend is opposite to what one usually sees in conventional-scale engines for which the power and torque increase approximately linearly with rpm before tailing off at the engine's maximum rated speed. One reason for this behavior is that the overall volumetric efficiency of the engine decreases with increasing engine speed, thereby reducing the amount of oxygen available for reaction in the combustion chamber. This is illustrated in Fig. 8, which shows that the delivery ratio (the ratio of the total mass of air ingested by the engine to the maximum mass that could possibly be ingested) decreases with increasing engine speed. The delivery ratio λ is defined as follows [29]:

$$\lambda = \dot{m}_a / \rho_a N V_d \tag{13}$$

where $\dot{m}_a$ is the mass flow rate of air ingested by the engine, ρ_a is the density of air, N is the engine speed, and V_d is the engine displacement. Figure 8 suggests that less energy is released per stroke at higher speeds, because less air (oxygen) is available to react with the fuel. The result is reduced torque and eventually reduced power. The delivery ratio is independent of the mixture setting.

The data in Fig. 9 show that cylinder head temperatures (CHT) and exhaust gas temperatures (EGT) increase monotonically with decreasing fuel/air ratio, providing further evidence that the equivalence ratio is significantly greater than one (i.e., rich) over the entire operating range of the engine. This suggests that chemical reaction rates are significantly lower than their peak values and that the decrease in torque with engine speed probably occurs because the overall Damkohler number (or the ratio of the time available for combustion to the time required to complete the chemical reaction) decreases with increasing engine speed. However, more detailed measurements of ignition timing and burning rate need to be made using cylinder pressure measurements.

The results presented so far illustrate that the engine's performance is heavily influenced by the fuel/air ratio, which

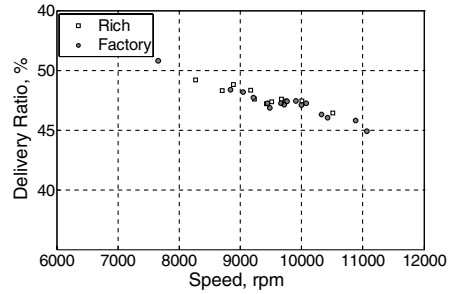

Fig. 8 Delivery ratio as a function of engine speed at WOT for two different mixture settings.

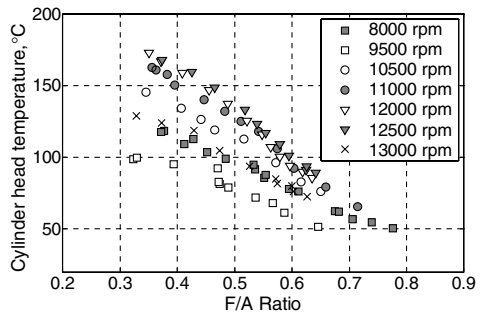

Fig. 9 Cylinder head temperature as a function of fuel/air ratio at WOT.

changes significantly over the operating range of the engine. Therefore, a final set of measurements was made to identify the optimum mixture settings associated with various operating speeds. This was accomplished by varying the mixture setting while adjusting the load to maintain constant engine speed. The results are presented in Fig. 10. They show that the peak power output of the engine is 159 W at 12,000 rpm. This is slightly greater than the value measured with the fixed needle-valve setting. Because the power output does not change much between 10,500 and 12,000 rpm, the data indicate that it may be advantageous to operate at 10,500 rpm in applications for which engine life is important. The peak power density of the engine is 1060 W/kg, which is comparable to that of a typical general aviation engine such as the Lycoming IO-370-2LA (134.4 kW, 133.8 kg).

Figure 10 shows that the BSFC approaches the same limiting value of 2 kg/kWh (corresponding to an efficiency of 8.3%) at all operating speeds: a 37% improvement over the value obtained without mixture control. Because aircraft range and endurance are directly proportional to engine efficiency, these data suggest that

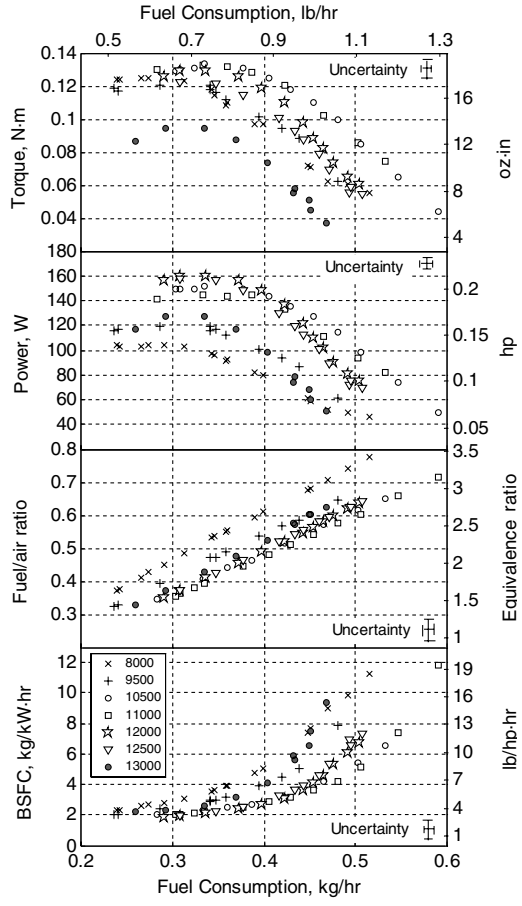

Fig. 10 Engine performance as a function of fuel flow rate at WOT.

Table 5 Effect of power system choice on small UAV range and endurance

Power System	η_{th}	Q_R	Range	Endurance (at 30 m/s)
Li-polymer battery with electric motor [32]	95	333	218	2
DARPA direct methanol fuel cell (1000 W · h/kg) with electric motor [33]	35	1000	267	2.47
150-g model engine (standard)	6	6061	278	2.57
150-g model engine with mixture control	8.2	6061	380	3.5
	%	W · h/kg	Km	Hr

controlling the mixture offers the potential to significantly improve UAV range and/or endurance. In addition, the fact that the minimum BSFC can be obtained at all operating speeds is advantageous, because it means that tradeoffs between efficiency and power output are not required. However, this overall level of efficiency (8%) is still much lower than that achieved by conventional-sized aircraft engines. For example, the Lycoming IO-370-2LA has a specific fuel consumption of 0.27 kg/kWh [30], which corresponds to an overall efficiency of approximately 30%. As a result, a UAV powered by the small engine tested here will be unable to achieve levels of range and/or endurance comparable with those achieved by larger vehicles with more efficient powerplants.

Nevertheless, this level of performance is still advantageous when compared with the performance of UAVs powered using batteries or fuel cells. The range of a small, fixed-wing UAV can be expressed in terms of the efficiency of the power plant η_{th}, along with the efficiency of the propulsion system (propeller) η_p, the heating value of the fuel, the lift/drag ratio of the vehicle, and the fuel mass fraction at takeoff using the Brequet range equation [31]:

$$\text{range} = \eta_p \eta_{th} (Q_R/g)(L/D)\, \ell n(1 + \chi_f) \tag{14}$$

Table 5 shows the range of various vehicles computed using Eq. (14) for a typical small UAV with $L/D = 8$, $\eta_p = 0.7$, and $\chi_f = 0.45$. The data show that improvements in range and/or endurance of approximately 35% can be achieved by implementing some sort of mixture control.

Finally, a careful examination of the data presented in Fig. 10 shows that the power output of the engine does, in fact, increase with engine speed (like conventional-sized engines) at constant mixture ratio. Therefore, the unusual shapes of the power curves presented in Figs. 5 and 6 (i.e., the decrease in power with engine speed) are a direct result of the variation in mixture ratio with engine speed. This can be seen more clearly in Fig. 11, which shows peak power and fuel/air ratio as a function of engine speed. The data show that peak power occurs when the fuel/air ratio is held constant at a value of approximately 0.4. Peak power decreases rapidly beyond speeds of 12,000 rpm, because of decreases in volumetric efficiency and Damkohler number.

IX. Conclusions

A dynamometer system suitable for measuring the performance of small internal-combustion engines has been constructed. The measurement system has been shown to be capable of measuring power output within ±9% and BSFC (or overall efficiency) within ±9%. This level of fidelity is sufficient to resolve the differences in performance between engines of different sizes to enable the development of scaling laws for small engine performance. The peak power output of the AP Engines Yellowjacket is 159 W (0.2 hp) at 12,000 rpm. This is 15% lower than the manufacturer's estimate of 0.25 hp but corresponds to a power density of 1060 W/kg, which is comparable to that of a conventional-sized piston aeroengine. However, the overall efficiency of the stock engine is approximately 6%, which is almost four times lower than the 30% achieved by conventional-scale piston aeroengines. This dramatic reduction in efficiency at small scales illustrates the difficulty of developing small UAVs with levels of range and/or endurance comparable to larger-scale vehicles and demonstrates the importance of understanding the factors that govern how engine performance scales with size. However, the data also indicate that improving the fuel delivery system by implementing some sort of mixture control can increase overall efficiency to 8%. This, in turn, could increase range and/or endurance of a small UAV by approximately 40% compared with a comparable battery-powered vehicle. Finally, the data indicate that engine performance varies significantly between engines of the same make and model. The reasons for this are not yet clear.

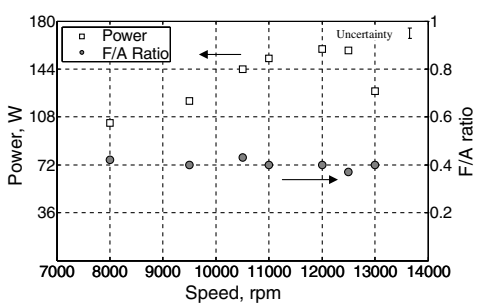

Fig. 11 Peak power output and corresponding fuel/air ratio as a function of engine speed at WOT.

Acknowledgments

This research work is supported by the U.S. Army Research Office through the Micro Air Vehicles, Multidisciplinary University Research Initiative (MAV MURI) program (grant no. ARMY-W911NF0410176) with Technical Monitor Gary Anderson. The authors would also like to thank Minor Appleman of the Naval Surface Warfare Center Carderock Division (NSWCCD) and Vince Castelli, formerly of NSWCCD, for partial support of this work during its early stages.

References

[1] Hill, P. G., and Peterson, C. R., *Mechanics and Thermodynamics of Propulsion*, Addison Wesley Longman, Reading, MA, 1965, p. 145.

[2] Lowry, J. T., "Fixed-Pitch Propeller/Piston Aircraft Operations at Partial Throttle," *Journal of Propulsion and Power*, Vol. 15, No. 4, 1999, pp. 497–503.

[3] Peterson, R. B., "Size Limits for Regenerative Heat Engines," *Microscale Thermophysical Engineering*, Vol. 2, No. 2, 1998, pp. 121–131.

[4] Cadou, C. P., "Reactive Processes in Micro-Scale Combustion Systems," Western States Section, Combustion Inst., Paper 03F-79, Los Angeles, 2003.

[5] Aichlmayr, H. T., Kittelson, D. B., and Zachariah, M. R., "Miniature Free-Piston Homogeneous Charge Compression Ignition Engine-Compressor Concept, Part 1: Performance Estimation and Design Considerations Unique to Small Dimensions," *Chemical Engineering Science*, Vol. 57, No. 19, Oct. 2002, pp. 4161–4171.

[6] Annen, K. D., Stickler, D. B., and Woodroffe, J., "Linearly-Oscillating Miniature Internal Combustion Engine (MICE) for Portable Electric Power," AIAA Paper 2003-1113, 2003.

[7] Epstein, A., and Senturia, S. D., "Macro Power from Micro Machinery," *Science*, Vol. 276, No. 5316, 1997, pp. 1211.

[8] Fu, K., Knobloch, A., Martinez, F., Walther, D., Fernandez-Pello, C., Pisano, A., Liepmann, D., Miyaska, K., and Maruta, K., "Design and Experimental Results of Small-Scale Rotary Engines," International Mechanical Engineering Conference and Exhibition, Paper IMECE2001/MEMS-23924, 2001.

[9] Papac, J., and Dunn-Rankin, D., "Combustion in a Centimeter-Scale Four-Stroke Engine," Western States Section, Combustion Inst.

Paper 04S-11, 2004.
[10] Papac, J., and Dunn-Rankin, D., "In Cylinder Pressure and Combustion Measurements in a Miniature Reciprocating Engine," *4th Joint Meeting of the U. S. Sections of the Combustion Institute*, Combustion Inst., Philadelphia, PA, 2005.
[11] Rais-Rohani, M., and Hicks, G., "Multidisciplinary Design and Prototype Development of a Micro Air Vehicle," *Journal of Aircraft*, Vol. 36, No. 1, 1999, pp. 227–234.
[12] Chinn, P. G. F., "Import Review," *Model Airplane News*, Vol. 56, No. 3, Mar. 1957, p. 28.
[13] Gierke, D., "Nelson Quarter .40," *Model Airplane News*, Vol. 126, No. 12, Dec. 1998, p. 88.
[14] Gierke, D., "We Test 10 .60 Engines: Which is Right for You?," *Model Airplane News*, Vol. 131, No. 5, May 2003, p. 28.
[15] Chinn, P., "Engine Review, O. S. Max 10 R/C," *Model Airplane News*, Vol. 73, No. 2, Aug. 1966, p. 24.
[16] Chinn, P., "Engine Review Webra .61 R/C," *Model Airplane News*, Vol. 93, No. 6, Dec. 1976, p. 20.
[17] Pond, S., and Gierke, D., "O.S .18TZ: A Weapon of Mass Combustion," *Radio Control Nitro*, Mar. 2005, pp. 90–92.
[18] Gierke, D., "Moki 1.20," *Model Airplane News*, Vol. 126, No. 10, Oct. 1998, p. 72.
[19] Heywood, J. B., *Internal Combustion Engine Fundamentals*, McGraw–Hill, New York, 1988, p. 84.
[20] Heywood, J. B., *Internal Combustion Engine Fundamentals*, McGraw–Hill, New York, 1988, p. 51.
[21] Cadou, C. P., Moulton, N., and Menon, S., "Performance Measurement and Scaling in Small Internal Combustion Engines," AIAA Paper 2003-0671, 2003.
[22] Gierke, David, "Part 1: Dynamometer and Engine Performance Analysis," *Flying Models*, June 1973, pp. 21–25.
[23] Gierke, D., "Part 2: Dynamometer and Engine Performance Analysis," *Flying Models*, July 1973, pp. 43–51.
[24] Gierke, D., "Part 3: Dynamometer and Engine Performance Analysis," *Flying Models*, July 1973, pp. 38–47.
[25] Anon., "Standard Test Method for Heat of Combustion of Liquid Hydrocarbon Fuels by Bomb Calorimeter," American Society for Testing and Materials Paper D240, 2002.
[26] Anon., "NIST Chemistry WebBook," *NIST Standard Reference Database No. 69* [online database], http://webbook.nist.gov/chemistry/ [cited 4 Oct. 2006].
[27] Anon., "Engine Power Test Code-Spark Ignition and Compression Ignition-Net Power Rating," Society of Automotive Engineers Paper J1349, June 1995.
[28] Anon., "Test Uncertainty," American Society of Mechanical Engineers Paper PTC 19.1-1998, 1998.
[29] Heywood, J. B., *Internal Combustion Engine Fundamentals*, McGraw–Hill, New York, 1988, p. 237.
[30] Anon., *Cessna 172S Pilot's Operating Handbook*, Cessna Aircraft, Wichita, KS, 2003.
[31] Hill, P. G., and Peterson, C. R., *Mechanics and Thermodynamics of Propulsion*, Addison Wesley Longman, Reading, MA, 1965, p. 145.
[32] Fernandez-Pello, A. C., "Micro-Power Generation Using Combustion: Issues and Approaches," *Proceedings of the Combustion Institute*, Vol. 29, Part 1, Combustion Inst., Pittsburgh, PA, 2002, pp. 883–899.
[33] Yao, S. C., Fedder, G. K., Tang, X., Hsieh, C. C., Alyousef, Y. M., Vladimer, M. L., and Amon, C. H., "Thermo-Fluids Considerations in the Development of a Silicon-Based Micro-Scale Direct Methanol Fuel Cell," *ASME-ZSIS International Thermal Science Seminar*, American Society of Mechanical Engineers, New York, 2004, pp. 171–80.

T. Lieuwen
Associate Editor